

Robustness of the flux-free sector of the Kitaev honeycomb against environment

Alexander Sattler¹ and Maria Daghofer¹

¹*Institut für Funktionelle Materie und Quantentechnologien, Universität Stuttgart, 70569 Stuttgart, Germany*
(Dated: July 10, 2025)

The Kitaev honeycomb model (KHM) consists of spin-1/2 particles on a honeycomb lattice with direction-dependent Ising-like interactions. It can alternatively be described in terms of non-interacting Majorana fermions, can be solved exactly, and has a quantum spin-liquid ground state. Open boundaries then host Majorana zero modes (MZMs) that are robust against some types of disorder. We analyze the fate of the MZMs when they couple to an environment via a Lindblad master equation. By computing the time evolution of the density matrix, we find that when decoherence occurs, the steady state is mostly the maximally mixed state. Among the few exceptions is a parameter regime that realizes the superconducting Kitaev chain model with periodic boundary conditions. We consistently observe a quantum Zeno effect in the density matrix as well as in the entropy and fidelity, while it is not found in the energy gap of some gapped spin liquids. We thus present a comprehensive overview over MZMs coupled to a spin bath that is relevant to proposals to detect MZMs of Kitaev layers on surfaces using scanning tunneling microscopy (STM).

I. INTRODUCTION

Topological order [1–5] has attracted substantial interest owing to its ability to exhibit exotic phenomena such as fractionalized excitations, anyonic quantum statistics, gapless edge modes, and ground-state degeneracies. Transitions from topologically ordered phases to topologically trivial ones are characterized by closing the bulk energy gap. Notably, the topological characteristics of these phases are intrinsically robust against certain types of disorder.

The stability of topological order and its hallmark features, such as edge states, is well established in closed quantum systems. However, because all physical systems are subject to some degree of environmental coupling, it becomes essential to understand how interactions with the environment affect these phases. In particular, the role of decoherence [6, 7] in topological systems remains insufficiently explored. Crucially, topological systems are not inherently robust to decoherence, raising fundamental questions about the stability of topological order in realistic, and therefore open, systems.

For the realization of topological quantum computing [8–16], it is crucial to understand the extent to which the topological protection observed in closed systems persists under realistic conditions involving coupling to an environment. MZMs, predicted in topological superconductors [17, 18], are candidates for realizing topological qubits [15, 19–21]. Topological qubits are generally expected to exhibit a degree of robustness against decoherence. However, while some studies [22, 23] support this view, others have demonstrated that MZMs can be susceptible to decoherence, both in general and specifically during braiding operations [23–28]. Furthermore, the B phase of the KHM with time-reversal symmetry breaking exhibits localized MZMs at its vortex excitations, indicating its potential for topological quantum computation [14, 15, 29, 30].

Quantum spin liquids (QSLs) [31] represent a phase

of matter that typically exhibits quantum fluctuations, frustration, long-range entanglement, fractionalized excitations, emergent gauge fields, and the absence of long-range magnetic order down to zero temperature. The KHM [29] is a rare example of an exactly solvable, strongly interacting two-dimensional system whose ground state is a topological QSL. This model consists of spin-1/2 particles arranged on a honeycomb lattice, interacting via direction-dependent Ising-like couplings. Under open boundary conditions (OBC), the KHM supports edge states that are MZMs [32, 33]. Its exact solvability facilitates detailed studies of diverse topological phases and quantum phase transitions, including Abelian, non-Abelian, chiral, and non-chiral phases.

STM has been proposed as a method to probe MZMs in the Kitaev QSL [34–38]. However, STM setups inherently involve interactions between the KHM monolayer and the underlying substrate, making it crucial to understand how the substrate affects the properties of the KHM. We utilize the Lindblad master equation (LME) [7] to analyze how the substrate influences the properties of the KHM.

Experimental realization of a Kitaev QSL remains challenging, as the Kitaev interaction in all materials studied so far is accompanied by additional competing interactions [38–40]. Nevertheless, monolayers of candidate Kitaev QSL materials have been successfully fabricated on surfaces [38, 41, 42]. A different route to MZMs are atomic spin chains on superconducting substrates, created using an STM setup [43, 44]. A theoretical model featuring MZMs in one-dimensional topological superconductors is the Kitaev chain (KC) [45]. While this appears at first sight to be quite a different setup from a QSL, some regimes of the KHM can be mapped onto the KC, which we will also discuss.

In Sec. II, we present the KHM Hamiltonian for a cylindrical geometry and introduce the LME. In Sec. III A, we discuss the time evolution of the density matrix, with particular focus on the steady state. Afterward, we consider the case $J_x = J_y = J_z$ of the KHM (see Eq. (1)).

First, in Sec. IIIB, we analyze the time evolution of the entropy and fidelity. Second, in Sec. IIIC, we elaborate on how the band structure evolves. Third, Sec. IIID, we characterize the time evolution towards the steady state with a relaxation time. In Sec. IIIE we discuss how the previously obtained results change when the coupling constants are not equal anymore. Finally, Sec. IV summarizes our findings and outlines promising directions for future studies.

II. MODEL AND METHODS

The Hamiltonian for the KHM [29] is given by

$$H = \sum_{\alpha \in \{x,y,z\}} \sum_{\langle i,j \rangle_{\alpha}} J_{\alpha} \sigma_i^{\alpha} \sigma_j^{\alpha}, \quad (1)$$

where the sum $\sum_{\langle i,j \rangle_{\alpha}}$ runs over all nearest-neighbor pairs connected by bonds of type α , and J_{α} denotes the corresponding coupling strength. Throughout this work, we adopt the convention $J_x + J_y + J_z = 1$ (with $\hbar = 1$). This bond-dependent Ising-like interaction can arise in certain materials [38–40] via the Jackeli-Khaliullin mechanism [46], and can lead to effective coupling parameters associated with the B phase of the KHM. Accordingly, our primary focus will be on the B phase, and in the following sections, we will primarily consider $J_x = J_y = J_z$. However, we will also, in some places, mention phases A_i with $i = x, y, z$ referring to the gapped spin liquids found for $J_i \gg J_{j \neq i}$.

Using a cylindrical geometry with zigzag edges in the KHM (see Fig. 1) takes advantage of its exact solvability to make calculations easier and allow MZMs to appear. The detailed derivation of the KHM Hamiltonian for this geometry and the flux-free sector can be found in Ref. [33]. The resulting Hamiltonian is

$$\begin{aligned} H = & \sum_{l=1}^L \sum_k \left(J_x - J_z \cos(k) \right) \left[\alpha_{(l,k)}^{\dagger} \alpha_{(l,k)} - \alpha_{(l,-k)} \alpha_{(l,-k)}^{\dagger} \right] \\ & + \frac{J_y}{2} \sum_{l=1}^{L-1} \sum_k \left[\alpha_{(l,-k)} \alpha_{(l+1,k)} - \alpha_{(l+1,-k)} \alpha_{(l,k)} \right. \\ & \quad - \alpha_{(l,k)}^{\dagger} \alpha_{(l+1,-k)}^{\dagger} + \alpha_{(l+1,k)}^{\dagger} \alpha_{(l,-k)}^{\dagger} + \alpha_{(l,-k)} \alpha_{(l+1,-k)}^{\dagger} \\ & \quad \left. - \alpha_{(l+1,k)}^{\dagger} \alpha_{(l,k)} - \alpha_{(l,k)}^{\dagger} \alpha_{(l+1,k)} + \alpha_{(l+1,-k)} \alpha_{(l,-k)}^{\dagger} \right] \\ & + J_z \sum_{l=1}^L \sum_k i \sin(k) \left[\alpha_{(l,-k)} \alpha_{(l,k)} - \alpha_{(l,k)}^{\dagger} \alpha_{(l,-k)}^{\dagger} \right], \end{aligned} \quad (2)$$

where L is the number of sites along the OBC direction, l indexes these sites, and $\alpha_{(l,k)}$ is the complex fermionic operator at site l .

This fermionic formulation of the KHM also illustrates that one can use the same model to investigate the KC. Setting $J_z = 0$ gives us KCs with OBC, while restricting the length of the cylinder to $L = 1$ leads to the KC with periodic boundary conditions (PBC). The same scenario

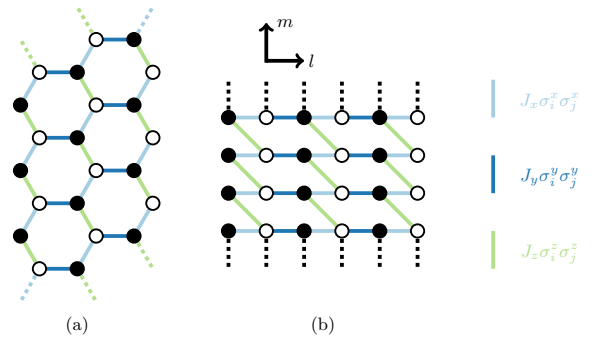


FIG. 1. This figure depicts two lattice structures, the KHM lattice (a) and the deformed brick-wall lattice (b), which are topologically equivalent. PBC are imposed along the m direction, indicated by dashed lines, while OBC are applied along the orthogonal l direction. The lattice sites are distinguished by their l values: black circles denote sites with odd l , whereas white circles denote sites with even l .

can also be achieved by setting $J_y = 0$, which yields L identical copies of the KC with PBC.

We use the Bogoliubov-de Gennes (BdG) formalism to obtain the bands of the closed KHM. Due to the redundancy arising from the introduction of hole operators, we exclude bands with negative energy to avoid double counting. Remaining bands are then labeled in ascending order, so that $n_{\text{band}} = 1$ corresponds to the lowest band with positive energy.

During the derivation of this Hamiltonian in Ref. [33], the fact that the ground state lies in the flux-free sector was exploited to eliminate quartic terms. This simplification raises questions about its suitability for calculating time evolution via the LME. While time evolution based on the LME generally requires considering the entire Hilbert space, extending beyond the flux-free sector introduces quartic terms. Based on Refs. [47–49], restricting the analysis to the flux-free sector may be a reasonable approximation, and we, therefore, adopt this simplest approach.

The presence of MZMs depends on both the coupling strengths and the edge structure, specifically on whether the geometry is zigzag or armchair [32, 33]. For the zigzag edge geometry analyzed here, the KHM exhibits MZMs in both the B phase and the A_y phase. These MZMs form a flat band at zero energy [50], however, modes at different edges interact for finite systems, leading to the finite-size effect of a nonzero energy, which decreases exponentially with increasing system size L .

To accurately model an STM setup, the interaction between the KHM monolayer and the surface must be taken into account. We employ an effective model that describes the KHM as an open quantum system interacting with the surface, which acts as its environment. The dynamics of open quantum systems are commonly described by master equations [7]. Lindblad [51] and Gorini, Kossakowski, and Sudarshan [52] derived the general structure of the generator \mathcal{L} , which describes the

Markovian time evolution of density matrices. The LME is given by

$$\dot{\rho} = \mathcal{L}(\rho) = i[H, \rho] + \gamma \sum_i \left(L_i \rho L_i^\dagger - \frac{1}{2} \{ L_i^\dagger L_i, \rho \} \right), \quad (3)$$

where L_i are the jump operators, $\gamma > 0$ the dissipation strength, and $\hbar = 1$. As an initial condition, we assume that the coupling between the system and its environment is switched on at $t = 0$. Derivations of the LME can be found in Refs. [6, 7, 51–56]. Details of the numerical methods employed are provided in Sec. A. The LME is employed to determine the time evolution of the eigenstates of the Hamiltonian in Eq. (2).

The aim is to compute the time evolution using the LME, with a focus on decoherence. The Pauli matrix σ^z is known to induce decoherence [7, 57–61]. After transformation with the same Jordan-Wigner transformation (JWT) applied during the derivation of the Hamiltonian [33], it corresponds to the number operator (up to factors), which then induces decoherence in the fermionic system [62–66]. The complete list of jump operators examined is in Tab. I. We employ one jump operator for each of the L sites along the OBC direction, with a uniform dissipation rate γ for each.

III. RESULTS

We first discuss the time evolution of density matrices in Sec. III A, then go to quantities like entropy and fidelity in Sec. III B, and finally discuss band structure and the spectral gap in Secs. III C and III D. We finally vary parameter of the Hamiltonian in Sec. III E.

A. Time evolution of density matrices – steady states

In this section, we discuss the time evolution of density matrices. The detailed features for the different jump operators, such as whether they cause decoherence, preserve the BdG-type particle-hole symmetry (PHS), and their steady states are discussed in Sec. B.

The steady state depends on k , J_α , L , and the jump operators (see Tab. II). Remarkably, fundamentally different sets of jump operators can yield the same steady state. Often, this steady state is the maximally mixed (mm) state,

$$\rho_{\text{mm}} = \frac{1}{2L} \mathbb{1}, \quad (4)$$

where $\mathbb{1}$ is the identity matrix. If ρ_{mm} is the steady state, it is unique, and this steady states can arise from quite different jump operators, for instance involving number operators, pair creation and annihilation operators, and incoherent hopping operators (see Tab. II). Although these jump operators, and also different parameters for

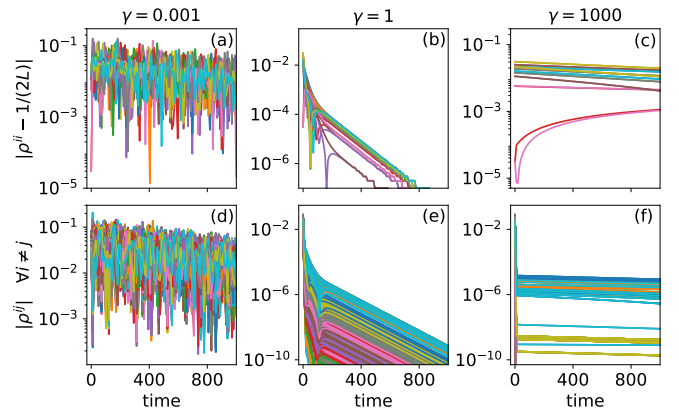


FIG. 2. Time evolution of the off-diagonal (bottom row) and diagonal (top row) elements of the density matrix ρ , shown relative to the steady state ρ_{mm} . The system parameters are $L = 10$, $J_x = J_y = J_z = 1/3$, $k = 1$, $n_{\text{band}} = 2$, and the jump operator L_{n-k}^{n+k} . The left, middle, and right columns correspond to $\gamma = 0.001$, $\gamma = 1$, and $\gamma = 1000$, respectively. The QZE is observable.

the Hamiltonian, can lead to distinct short-time dynamics, the long-time behavior is largely similar due to the common steady state.

The steady states are identical for all sets of jump operators based on number operators, although the density matrices differ over time (see Tab. II). This leads to several conclusions. First, the steady state is independent of whether the BdG-type PHS is preserved (L_n and L_{n-k}^{n+k}) or broken (L_{n+k} and L_{n-k}). Second, for the steady state, it does not matter if the jump operators act on the entire Nambu spinor (L_n and L_{n-k}^{n+k}) or only half of the Nambu spinor (L_{n+k} and L_{n-k}). Third, it does not matter whether we treat number operators with $\pm k$ via two jump operators per site (L_{n-k}^{n+k}) or use a single jump operator per site (L_n).

In addition to sharing a steady state, those jump operators that preserve the BdG-type PHS also have quite similar short-time evolution. Consequently, as long as ρ_{mm} is the steady state (see Tab. II), the time evolution is similar for L_n , L_{n-k}^{n+k} , L_p , $L_{p,c}^{\text{pa}}$, and incoherent jump operators. Remarkably, this implies that the time evolution is comparable for microscopically quite different jump operators based on number operators, pair creation and annihilation operators, as well as incoherent hopping operators.

While the differences between these sets of jump operators are minimal for the most symmetric case $J_x = J_y = J_z$, they can become larger for the three A_i phases. A general trend is that as the disparity between the coupling constants J_α increases, so do the differences between the dynamics induced by various sets of jump operators. Another trend is that differences also increase with increasing γ , however, they typically remain small as long as $\gamma < J_\alpha$.

On the other hand, steady states can differ between OBC and PBC for the parameter regimes modeling the

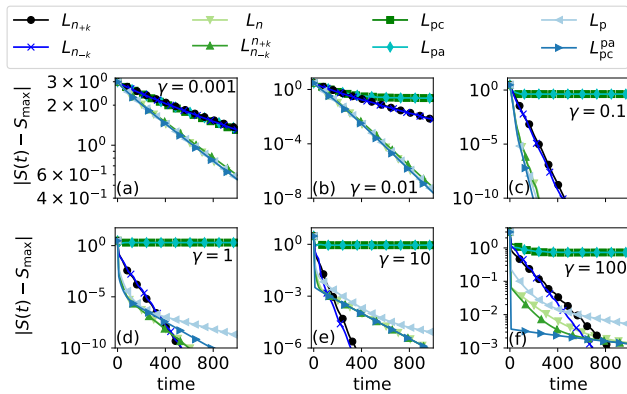


FIG. 3. The time evolution of the entropy for different jump operators (definitions in Tab. I), where each panel corresponds to a different γ . The entropy is shifted by S_{\max} , the steady-state entropy when the system reaches the state ρ_{mm} (see Eq. (6)). The parameters are $L = 10$, $J_x = J_y = J_z = 1/3$, $n_{\text{band}} = 2$, and $k = 1$. The steady states are listed in Tab. II. Unlike the other jump operators shown in this figure, the steady states for L_{pc} and L_{pa} are not ρ_{mm} , which explains why $|S(t) - S_{\max}|$ does not vanish over time.

KC. This distinction is evident in Tab. II by comparing the steady states for $J_z = 0$ (KC with OBC), for $L = 1$ (KC with PBC), and for $J_y = 0$ (L identical copies of the KC with PBC).

We find that decoherence can occur independently of the preservation of BdG-type PHS, as detailed in Tab. I. Specifically, all combinations are possible: decoherence with preservation of BdG-type PHS, decoherence with broken BdG-type PHS, absence of decoherence with preservation of BdG-type PHS, and absence of decoherence with broken BdG-type PHS.

Time evolution of density-matrix elements shows a quantum Zeno effect (QZE) [7, 67] for every set of jump operators considered. This phenomenon is illustrated in Fig. 2, where it can be observed by comparing the different columns. Comparison between the left and middle columns demonstrates that increasing γ accelerates the approach to the steady state. Conversely, comparison between the middle and right columns shows that further increasing γ slows convergence again. The fastest relaxation to the steady state for $J_x = J_y = J_z$ occurs roughly when $J_\alpha \sim \gamma$. As the differences among the couplings J_α increase, the position of this minimum shifts.

B. Entropy and fidelity

The time evolution of the density matrix, which transitions from an initial eigenstate to a typically mixed steady state, can be characterized by computing the von Neumann entropy

$$S(t) = -\text{Tr}[\rho(t) \ln(\rho(t))]. \quad (5)$$

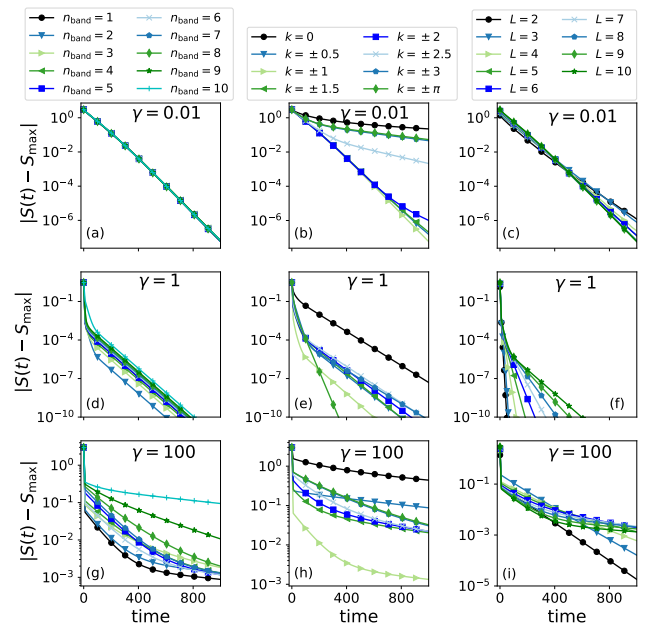


FIG. 4. Time evolution of the entropy, shifted by its steady-state value (see Eq. (6)), is shown for different bands (left column), k values (middle column), and finite-size effects (right column). Each row displays the time evolution for a different γ value. The parameters, if not varied, are $L = 10$, $J_x = J_y = J_z = 1/3$, $n_{\text{band}} = 2$, $k = 1$, and L_{n-k}^{n+k} .

In this section, we focus exclusively on the most common steady state, ρ_{mm} (see Tab. II), which has maximum achievable entropy

$$S(\rho_{\text{mm}}) = \ln(2L) = S_{\max}. \quad (6)$$

Consequently, as long as the steady state is ρ_{mm} , the entropy evolution converges to the same value regardless of the initial density matrix or jump operator. This section discusses how fast this limit is approached with various coupling to the environment in the case $J_x = J_y = J_z$, while Sec. III E explores the impact of non-identical coupling parameters.

In the case of $\gamma < J_\alpha$, the time evolution of the entropy is nearly identical for all jump operators from Tab. I that preserve the BdG-type PHS, as shown in Fig. 3. This similarity is remarkable, given that the physical processes described by these jump operators are microscopically quite distinct, and it is a direct consequence of the similarities in $\rho(t)$ discussed in Sec. III A. While differences emerge for $\gamma > J_\alpha$, they remain weak compared to the variations in entropy when k changes (see Fig. 4).

A QZE consistently occurs in $S(t)$, as seen in Figs. 3 and 4. As seen Sec. III A for the γ -dependence of $\rho(t)$, the fastest approach to the steady-state value of the entropy occurs approximately when $J_\alpha \sim \gamma$. Starting from $J_\alpha \sim \gamma$, either increasing or decreasing γ causes the time evolution to slow down. Furthermore, the kink in $S(t)$ that occurs for $\gamma \gg J_\alpha$ is a direct consequence of the kink

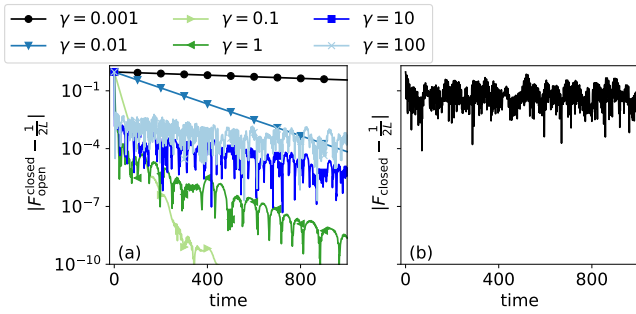


FIG. 5. (a) Time evolution of the fidelity defined in Eq. (7b), shifted by its steady-state value from Eq. (8), for different values of γ . For comparison, (b) shows the fidelity for the unitary time evolution (i.e., $\gamma = 0$) as defined in Eq. (7a). The parameters are $J_x = J_y = J_z = 1/3$, $L_{n_{\pm k}}^{n_{\pm k}}$, $L = 10$, $n_{\text{band}} = 2$, and $k = 1$.

in $\rho(t)$, as shown in Fig. 2(f).

While n_{band} and L have a negligible impact on the entropy for $\gamma < J_\alpha$ (see Figs. 4(a) and 4(c)), differences begin to emerge as γ increases (see Figs. 4(g) and 4(i)).

In contrast, the entropy shows a strong dependence on k for all values of γ (see Figs. 4(b), 4(e) and 4(h)). No general pattern emerges that would allow us to predict which k values lead to a faster or slower increase in entropy relative to others.

The Uhlmann fidelity $F(t)$ quantifies the similarity between two density matrices:

$$F_{\text{closed}}(t) = \text{Tr}[\rho(t=0) \cdot \rho_{\text{closed}}(t)], \quad (7a)$$

$$F_{\text{open}}^{\text{closed}}(t) = \text{Tr}[\rho_{\text{open}}(t) \cdot \rho_{\text{closed}}(t)], \quad (7b)$$

where $\rho(t=0)$ is the initial density matrix of the closed system, $\rho_{\text{open}}(t)$ represents the time evolution in an open system ($\gamma > 0$), and $\rho_{\text{closed}}(t)$ describes the time evolution in a closed system ($\gamma = 0$). For the most common steady state, ρ_{mm} (see Tab. II), we obtain

$$F_{\text{open}}^{\text{closed}}(\rho_{\text{open}} = \rho_{\text{mm}}) = \frac{1}{2L}. \quad (8)$$

The KHM with full PBC in both directions was analytically studied in Ref. [49] and an expression for $F_{\text{open}}^{\text{closed}}$ was derived. Additionally, Ref. [64] calculates the fidelity for various spin chains and a two-dimensional Bose gas. Both references obtain the same analytical expression for the fidelity under the assumptions of weak coupling ($\gamma \ll J_\alpha$). Motivated by the analytical form of the fidelity, we investigate whether our numerically computed fidelities can be accurately described by such an analytical expression. Thus, we use their expression for the fidelity as a fitting function, adapted by including a finite-size effect term (which depends on the steady state (ss)):

$$F_{\text{fit}}(t) = Ct^{-b}e^{-at} + \frac{1}{2L} \quad \text{if} \quad \rho_{\text{ss}} = \rho_{\text{mm}}. \quad (9)$$

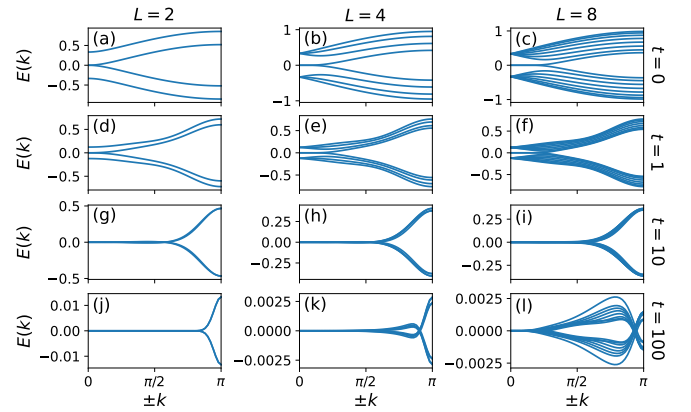


FIG. 6. Finite-size effects in the time evolution of the band structure for the parameters $J_x = J_y = J_z = 1/3$, $L_{n_{\pm k}}^{n_{\pm k}}$, and $\gamma = 1$. Each column displays the band structure for a specific value of L (above the top row), while each row represents the band structure at a particular time point (to the right of the rightmost column).

We also apply this fitting function to the entropy.

It turns out that this fitting function can be applied to both $F_{\text{open}}^{\text{closed}}$ and the entropy provided that $\gamma \ll J_\alpha$. Aside from this condition, it is valid for all parameter regimes, including, in particular, for the MZM. This extends previous results, as Ref. [49] focuses exclusively on fidelity for the KHM with PBC in both directions, i.e., without MZMs. The necessity of the condition $\gamma \ll J_\alpha$ is consistent with the approximations employed in the analytical derivations. However, there is no sharp threshold in the ratio γ/J_α that delineates where the fitting function becomes invalid. Instead, fitting errors increase gradually as γ/J_α grows, until a critical value is reached beyond which the fitting procedure fails to converge. Fit parameters vary strongly with the Hamiltonian and LME parameters, preventing clear or consistent patterns from emerging.

A typical example of the time evolution of the fidelity is shown in Fig. 5(a). For weak coupling $\gamma \ll J_\alpha$, the fidelity follows a straight line and becomes, as expected, constant in the limit $\gamma \rightarrow 0$. For larger values of γ , the fidelity no longer follows a straight line due to variations occurring in the density matrices of the closed KHM, as shown in Fig. 5(b). Furthermore, the kink that appears in the density matrices for $\gamma \gg J_\alpha$ (see Fig. 2(f)) also emerges in the fidelity.

While the straight lines in Fig. 5(a) can be well described by Eq. (9), once the kink and strong variations appear, the time evolution becomes more complex than can be captured by the analytically derived function of Refs. [49, 64].

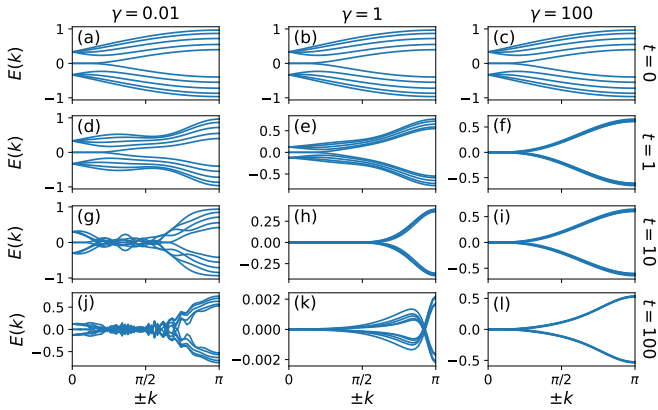


FIG. 7. Influence of γ on the time evolution of the band structure for $J_x = J_y = J_z = 1/3$, $L = 5$, and L_{n+k}^{n+k} . Each column shows the band structure for a specific value of γ (above the top row), while each row corresponds to a particular time point (to the right of the rightmost column). The QZE is observable.

C. Time evolution of the band structure

In this section, we analyze the time evolution of the band structure for $J_x = J_y = J_z$. A complete list of the jump operators considered here is provided in Tab. I.

As discussed above and summarized in Tab. II, the steady state is in most cases ρ_{mm} . The energy associated with ρ_{mm} is independent of all Hamiltonian parameters and is identical across all bands:

$$E(\rho_{\text{mm}}) = \text{Tr}[\rho_{\text{mm}} H_{\text{KHM}}] = 0, \quad (10)$$

as a consequence of BdG-type PHS. In such cases, all energies decay to zero over time. Thus, the key remaining questions concern the short-time dynamics and the decay rate of the energies. Only in those cases where the steady state deviates from ρ_{mm} do energies remain nonzero at all times.

When ρ_{mm} is the steady state, the rate at which energies decay to zero depends sensitively on whether the jump operators preserve or break the BdG-type PHS. In cases where PHS is broken (e.g., L_{n+k} or L_{n-k}), decay is significantly slower. This is expected, as such operators act only on the $+k$ or $-k$ modes, respectively, affecting only half of the BdG degrees of freedom. In contrast, jump operators that preserve BdG-type PHS include both $+k$ and $-k$ modes (e.g., L_{n+k}^{n+k} or L_n), acting on all BdG degrees of freedom and facilitating faster relaxation.

Comparing L_{n+k} and L_{n-k} reveals that their band structures are related by a sign change in energy. Similarly, the band structures of L_{pc} and L_{pa} are connected through the same energy sign change.

The way operators L_{n+k} and L_{n-k} , or L_{pc} and L_{pa} , which individually break BdG-type PHS, are combined to form PHS preserving jump operators influences the system's time evolution. The differences between L_n and

L_{n-k} are minimal, whereas the differences between $L_{\text{pc}}^{\text{pa}}$ and L_{p} are more substantial. For example, at $t = 1$, an energy gap is present for L_{p} , while no such gap exists for $L_{\text{pc}}^{\text{pa}}$. Furthermore, comparing L_n and L_{n-k} with $L_{\text{pc}}^{\text{pa}}$ and L_{p} shows that the energy levels approach $E = 0$ more quickly for $L_{\text{pc}}^{\text{pa}}$ and L_{p} .

Figure 6 shows that finite-size effects have a weak impact on the time evolution. The bandwidth remains nearly unchanged between $L = 4$ and $L = 8$, indicating that the approach of energy levels toward zero is only weakly dependent on system size. The bottom row of the figure highlights the emergence of an energy gap at specific k values. As L increases, this gap becomes apparent at a growing number of k points.

The ratio J_α/γ significantly impacts the time evolution of the band structure, as shown in Fig. 7. The QZE consistently occurs, as evidenced by the faster reduction of the energies for $\gamma = 1$ compared to $\gamma = 100$. The fastest approach to $E = 0$ occurs, similar to observations made above, when $\gamma \sim J_\alpha$. For $\gamma \ll J_\alpha$, time evolution closely resembles that of the closed system, with one crucial difference: the energies gradually decrease toward zero. As γ increases toward J_α , the energies approach $E = 0$ more rapidly. In the regime $\gamma \gg J_\alpha$, the time evolution again approximates that of the closed system, but with two key differences: First, the energies decrease very slowly toward the steady-state energy. Second, the energies of the different bands become nearly identical immediately after coupling to the environment is switched on. This remains essentially the only change over long timescales, as seen by the similarity between the band structures at $t = 1$ and $t = 100$. In contrast, for $\gamma \ll J_\alpha$, the energy bands remain well-separated over longer times. The bandwidth is nearly identical in both the $\gamma \ll J_\alpha$ and $\gamma \gg J_\alpha$ regimes.

D. Spectral gap

The long-term behavior can be characterized by relaxation times. For the LME, the eigenvalues λ_α of the \mathcal{L} can be used to determine a relaxation time, since these eigenvalues appear in the exponential function of Eq. (A2). The real parts $\text{Re}(\lambda_\alpha)$ indicate the rate at which the steady state is approached. The long-time dynamics are governed by the slowest exponential decay, which directly leads to

$$\frac{1}{\tau} = \Delta := - \max_{\text{Re}[\lambda_\alpha] \neq 0} \text{Re}(\lambda_\alpha), \quad (11)$$

where the inverse of the spectral gap Δ defines the relaxation time τ [57, 58, 60, 68, 69].

The ratio J_α/γ significantly influences τ . There is a QZE in τ for all analyzed jump operators and Hamiltonian parameters, with a typical example shown in Fig. 8. The robustness reaches a minimum at $\gamma \sim J_\alpha$ for $J_x = J_y = J_z$, consistent with the results for all other analyzed quantities.

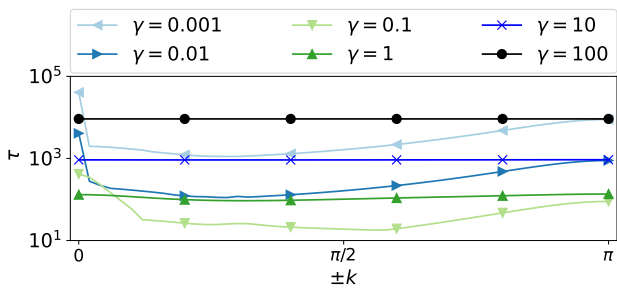


FIG. 8. The dependence of τ , as defined in Eq. (11), on k is shown for various values of γ . The parameters are $L_{n_{\pm k}}^{n_{\pm k}}$, $L = 10$, and $J_x = J_y = J_z = 1/3$. The QZE always occurs for τ .

The variation of τ with k is governed by both γ and the choice of jump operators. The value of k at which $\tau(k)$ attains its maximum or minimum depends on the parameters of the Hamiltonian and the jump operators. Both minima and maxima can occur at any value of k . While for $\gamma \ll J_\alpha$, τ can change significantly with variations in k , for $\gamma \gg J_\alpha$, τ becomes independent of k for jump operators that induce decoherence, as shown for one example in Fig. 8. In contrast, for jump operators that do not induce decoherence, τ exhibits a strong k -dependence across all values of γ . Additionally, changes in the degeneracy of the eigenvalue $\lambda_0 = 0$ (denoted as $\text{deg}(\lambda_0)$), i.e., the number of steady states, can depend on k for some jump operators and lead to a divergence of τ (see Fig. 9).

τ can be identical for some physically distinct jump operators but varies strongly for others. τ is identical for L_{pc} and L_{pa} , as well as for $L_{n_{+k}}$ and $L_{n_{-k}}$, however, this is not unexpected since the band structures are related through a sign change in these cases. Differences between various sets of jump operators are generally more pronounced at weaker γ . For $\gamma \gg J_\alpha$, τ becomes identical (and is already nearly identical for $\gamma \approx J_\alpha$) for several combinations (e.g., for $L_{n_{-k}}^{n_{+k}}$, L_n , and $L_{\text{pc}}^{\text{pa}}$, or, another example, L_{pc} , L_{pa} , $L_{n_{+k}}$, and $L_{n_{-k}}$). Notably, L_p remains distinct due to differences in $\text{deg}(\lambda_0)$. For τ , significant differences emerge between jump operators that preserve and those that break the BdG-type PHS.

Finite-size effects, as shown in Fig. 9, are weak for $\gamma \ll J_\alpha$ (except for $k \approx 0$), but τ can vary by several orders of magnitude for $\gamma \gg J_\alpha$. While for $\gamma \ll J_\alpha$ increasing the system size L slightly decreases τ (except for $k \approx 0$), for $\gamma \gg J_\alpha$ increasing L strongly increases τ . An exception occurs for $L = 1$, where τ deviates from the trend due to a k -dependent $\text{deg}(\lambda_0)$, unlike for $L \geq 2$.

E. Variation of the coupling constants

We previously focused mostly on the case $J_x = J_y = J_z$ and now briefly examine how the results change when the

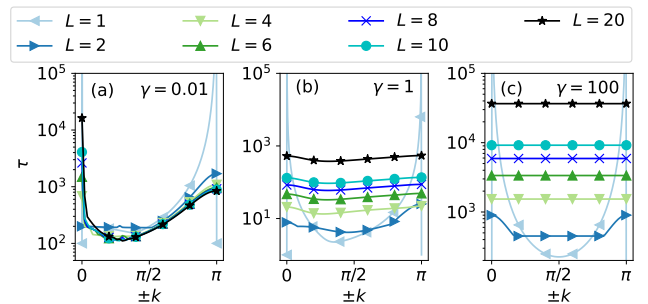


FIG. 9. Finite-size effects for τ , as defined in Eq. (11), are shown. The parameters are $L_{n_{\pm k}}^{n_{\pm k}}$ and $J_x = J_y = J_z = 1/3$, and the value of γ is indicated in each figure.

couplings are not identical.

For unequal coupling parameters J_x , J_y , and J_z , the entropy exhibits a complex and largely unpredictable time evolution. This arises from the fact that changing a single parameter can have varying effects on the entropy, depending on the values of other parameters. Such behavior is observed across all parameters, including J_α , k , n_{band} , L , and the choice of jump operators. In particular, the entropy can exhibit fundamentally different behavior for varying values of γ . As a result, varying a single parameter can lead to either nearly identical or fundamentally different entropy time evolution.

Several conclusions follow: There is no clear relation between the energy gap of the closed system and the approach to the steady state in the open system. The presence or absence of MZMs has no relation to the rate of entropy growth. No systematic difference is found in the entropy increase rate between the KHM and the KC. Different boundary conditions (OBC or PBC) for the KC can lead to both similar and distinct entropy dynamics. Entropy time evolution shows no qualitative distinction between MZMs and other energy bands.

Everything discussed above regarding the entropy also applies to τ . However, one clear pattern is observed for τ , which increases as J_y decreases and ultimately diverges as J_y approaches zero, due to a change in $\text{deg}(\lambda_0)$ (see Tab. II). The only effect that consistently appears for both the entropy and τ is the QZE.

Lastly, we examine the time evolution of the band structure under varying coupling constants. Small changes in the couplings J_α can give rise to distinct time evolutions, such as strong variations in the timescales over which energy gaps close. Quantitatively (e.g., see the discussion on comparisons between various jump operators in Sec. III C), the same effects occur as for identical couplings, but the actual values of the energies depend strongly on the specific values of the J_α . For example, the rate at which the energies decrease toward zero in cases where ρ_{mm} is the steady state depends strongly on the couplings J_α but consistently exhibits the QZE. However, not all features of the band structure show the QZE, for instance, the energy gap in the A_x phase exhibits

QZE, whereas in the A_y and A_z phases, it does not. Despite identical band structures in the closed system, the time evolution differs significantly between the A_x and A_z phases. For example, the energy gap in A_x remains open for several orders of magnitude longer. Finite-size effects, which strongly depend on γ , J_α , and the jump operator, influence the energy gap lifetime, which decreases with increasing system size L , approaching a nonzero value.

IV. DISCUSSION AND CONCLUSIONS

We have investigated the flux-free sector of the KHM under environmental coupling. This was motivated by the prediction that signatures of MZMs can be measured with an STM [34–38]. However, in an STM setup, there is an unavoidable interaction between the surface and the KHM, which requires analyzing the KHM under environmental coupling. To do this, we have utilized the LME, focusing on jump operators that lead to decoherence, to analyze the time evolution of the entropy and band structure, as well as to calculate the spectral gap.

In addition to the expected decoherence induced by number operators, jump operators based on pair creation/annihilation or incoherent hopping also cause decoherence, so that the steady state is in most cases the maximally mixed state. Exceptions occur for $J_y = 0$ or $L = 1$, which correspond to KCs with PBC. Further, jump operators consisting purely of pair creation or pair annihilation as well as specific incoherent hoppings produce steady states that are not maximally mixed, but have non-vanishing off-diagonal elements in the density matrix.

Variations in the couplings J_α can lead to significant differences in τ and in the time evolution of the band structure, the entropy, and the fidelity. However, in most cases, the steady state does not depend on the couplings J_α , and thus the strong differences only occur on short time scales. No simple patterns emerge that would allow us to predict whether a variation in J_α leads to a faster or slower approach to the steady state. However, some statements can be made, e.g., the energy gap closes significantly faster in the A_z phase compared to the A_x phase.

The KHM Hamiltonian we investigated reduces to that of a KC for certain parameter choices, with PBC or OBC depending on the parameters selected. These parameter sets are among those that have an impact on time evolution, but one cannot say that the KHM is generally more

or less robust than the KC. However, the KC with PBC is a special case in which decoherence does not lead to a maximally mixed steady state.

Under variation of γ in the LME, a QZE usually occurs with a minimum in robustness at $J \sim \gamma$ for $J = J_x = J_y = J_z$. The QZE always occurs for the entropy, fidelity, and $\rho(t)$, but not for all features of the band structure: in the gapped spin liquids A_y and A_z , there is no QZE in the lifetimes of the energy gaps.

As the system evolves toward a maximally mixed steady state, the energies of all bands converge to zero. This causes the energy gap to close and the topological features of the band structure to vanish, eliminating any distinction between the MZM and the other bands. This indicates that a topological phase transition occurs over time. However, precisely determining this transition requires the evaluation of a topological invariant, which is beyond the scope of this work but is an interesting topic for future research.

Proposals for detecting the topological signatures of the KHM via STM [34–38] fundamentally rely on the coexistence of a bulk energy gap and gapless edge states. As the energy gap closes over time, the substrate’s coupling to the Kitaev monolayer must remain sufficiently weak to prevent rapid relaxation into the maximally mixed steady state, thereby preserving the conditions necessary for STM-based observation of topological signatures.

While this work focuses on zigzag edges, armchair edges [32, 33] represent an alternative, and it would be valuable to examine how edge geometry affects the time evolution. Future studies could also use the time evolution of the density matrix to calculate observables such as spin expectation values, spin-spin correlations, or the plaquette operator. As pure KHM systems are unlikely to be realized experimentally [38, 39], it is of interest to extend the model by incorporating additional interactions, for example by including Heisenberg couplings.

ACKNOWLEDGMENTS

The authors acknowledge support by the state of Baden-Württemberg through bwHPC.

V. REFERENCES

-
- [1] F. D. M. Haldane, Nobel Lecture: Topological quantum matter, *Rev. Mod. Phys.* **89**, 040502 (2017).
 - [2] X.-G. Wen, Colloquium: Zoo of quantum-topological phases of matter, *Rev. Mod. Phys.* **89**, 041004 (2017).
 - [3] C.-K. Chiu, J. C. Y. Teo, A. P. Schnyder, and S. Ryu, Classification of topological quantum matter with symmetries, *Rev. Mod. Phys.* **88**, 035005 (2016).
 - [4] X.-L. Qi and S.-C. Zhang, Topological insulators and superconductors, *Rev. Mod. Phys.* **83**, 1057 (2011).
 - [5] M. Z. Hasan and C. L. Kane, Colloquium: Topological insulators, *Rev. Mod. Phys.* **82**, 3045 (2010).
 - [6] K. Hornberger, *Entanglement and Decoherence: Founda-*

- tions and Modern Trends* (Springer Berlin, Heidelberg, 2009) Chap. 5 Introduction to Decoherence Theory, Lecture Notes in Physics 768; Chapter 5 Introduction to Decoherence Theory.
- [7] H.-P. Breuer and F. Petruccione, *The Theory of Open Quantum Systems* (Oxford University Press, 2007).
- [8] D. Suter and G. A. Álvarez, Colloquium: Protecting quantum information against environmental noise, *Rev. Mod. Phys.* **88**, 041001 (2016).
- [9] I. L. Chuang, R. Laflamme, P. W. Shor, and W. H. Zurek, Quantum computers, factoring, and decoherence, *Science* **270**, 1633 (1995).
- [10] A. Beige, D. Braun, B. Tregenna, and P. L. Knight, Quantum computing using dissipation to remain in a decoherence-free subspace, *Phys. Rev. Lett.* **85**, 1762 (2000).
- [11] D. P. DiVincenzo, The physical implementation of quantum computation, *Fortschritte der Physik* **48**, 771 (2000).
- [12] T. D. Ladd, F. Jelezko, R. Laflamme, Y. Nakamura, C. Monroe, and J. L. O'Brien, Quantum computers, *Nature* **464**, 45 (2010).
- [13] D. P. DiVincenzo, Two-bit gates are universal for quantum computation, *Phys. Rev. A* **51**, 1015 (1995).
- [14] V. Lahtinen and J. K. Pachos, A short introduction to topological quantum computation, *SciPost Phys.* **3**, 021 (2017).
- [15] C. Nayak, S. H. Simon, A. Stern, M. Freedman, and S. Das Sarma, Non-Abelian anyons and topological quantum computation, *Rev. Mod. Phys.* **80**, 1083 (2008).
- [16] A. Steane, Quantum computing, *Reports on Progress in Physics* **61**, 117 (1998).
- [17] J. Alicea, New directions in the pursuit of Majorana fermions in solid state systems, *Reports on Progress in Physics* **75**, 076501 (2012).
- [18] M. Sato and Y. Ando, Topological superconductors: a review, *Reports on Progress in Physics* **80**, 076501 (2017).
- [19] C. W. J. Beenakker, Search for Majorana fermions in superconductors, *Annual Review of Condensed Matter Physics* **4**, 113 (2013).
- [20] J. Alicea, Y. Oreg, G. Refael, F. von Oppen, and M. P. A. Fisher, Non-Abelian statistics and topological quantum information processing in 1D wire networks, *Nature Physics* **7**, 412 (2011).
- [21] C. W. J. Beenakker, Search for non-Abelian Majorana braiding statistics in superconductors, *SciPost Phys. Lect. Notes* , 15 (2020).
- [22] M. Cheng, R. M. Lutchyn, and S. Das Sarma, Topological protection of Majorana qubits, *Phys. Rev. B* **85**, 165124 (2012).
- [23] Y. Hu, Z. Cai, M. A. Baranov, and P. Zoller, Majorana fermions in noisy Kitaev wires, *Phys. Rev. B* **92**, 165118 (2015).
- [24] J. C. Budich, S. Walter, and B. Trauzettel, Failure of protection of Majorana based qubits against decoherence, *Phys. Rev. B* **85**, 121405 (2012).
- [25] F. L. Pedrocchi, N. E. Bonesteel, and D. P. DiVincenzo, Monte Carlo studies of the self-correcting properties of the Majorana quantum error correction code under braiding, *Phys. Rev. B* **92**, 115441 (2015).
- [26] F. L. Pedrocchi and D. P. DiVincenzo, Majorana braiding with thermal noise, *Phys. Rev. Lett.* **115**, 120402 (2015).
- [27] G. Goldstein and C. Chamon, Decay rates for topological memories encoded with Majorana fermions, *Phys. Rev. B* **84**, 205109 (2011).
- [28] D. Rainis and D. Loss, Majorana qubit decoherence by quasiparticle poisoning, *Phys. Rev. B* **85**, 174533 (2012).
- [29] A. Kitaev, Anyons in an exactly solved model and beyond, *Annals of Physics* **321**, 2 (2006).
- [30] A. Kitaev, Fault-tolerant quantum computation by anyons, *Annals of Physics* **303**, 2 (2003).
- [31] L. Balents, Spin liquids in frustrated magnets, *Nature* **464**, 199 (2010).
- [32] M. Thakurathi, K. Sengupta, and D. Sen, Majorana edge modes in the Kitaev model, *Phys. Rev. B* **89**, 235434 (2014).
- [33] T. Mizoguchi and T. Koma, Majorana edge magnetization in the Kitaev honeycomb model, *Phys. Rev. B* **99**, 184418 (2019).
- [34] J. Feldmeier, W. Natori, M. Knap, and J. Knolle, Local probes for charge-neutral edge states in two-dimensional quantum magnets, *Phys. Rev. B* **102**, 134423 (2020).
- [35] M. Udagawa, S. Takayoshi, and T. Oka, Scanning tunneling microscopy as a single Majorana detector of Kitaev's chiral spin liquid, *Phys. Rev. Lett.* **126**, 127201 (2021).
- [36] E. J. König, M. T. Randeria, and B. Jäck, Tunneling spectroscopy of quantum spin liquids, *Phys. Rev. Lett.* **125**, 267206 (2020).
- [37] S.-S. Zhang, G. B. Halász, and C. D. Batista, Probing chiral Kitaev spin liquids via dangling boundary fermions, *npj Quantum Materials* **10**, 59 (2025).
- [38] Y. Matsuda, T. Shibauchi, and H.-Y. Kee, Kitaev quantum spin liquids (2025), arXiv:2501.05608 [cond-mat.str-el].
- [39] S. Mandal, A primer on Kitaev model: basic aspects, material realization, and recent experiments, *Journal of Physics: Condensed Matter* **37**, 193002 (2025).
- [40] S. M. Winter, A. A. Tsirlin, M. Daghofer, J. van den Brink, Y. Singh, P. Gegenwart, and R. Valenti, Models and materials for generalized Kitaev magnetism, *Journal of Physics: Condensed Matter* **29**, 493002 (2017).
- [41] Z. Wang, L. Liu, H. Zheng, M. Zhao, K. Yang, C. Wang, F. Yang, H. Wu, and C. Gao, Direct observation of the mottness and p-d orbital hybridization in the epitaxial monolayer α -RuCl₃, *Nanoscale* **14**, 11745 (2022).
- [42] Y. Kohsaka, S. Akutagawa, S. Omachi, Y. Iwamichi, T. Ono, I. Tanaka, S. Tateishi, H. Murayama, S. Suet-sugu, K. Hashimoto, T. Shibauchi, M. O. Takahashi, S. Nikolaev, T. Mizushima, S. Fujimoto, T. Terashima, T. Asaba, Y. Kasahara, and Y. Matsuda, Imaging quantum interference in a monolayer Kitaev quantum spin liquid candidate, *Phys. Rev. X* **14**, 041026 (2024).
- [43] R. Lo Conte, J. Wiebe, S. Rachel, D. K. Morr, and R. Wiesendanger, Magnet-superconductor hybrid quantum systems: a materials platform for topological superconductivity, *La Rivista del Nuovo Cimento* **47**, 453 (2024).
- [44] S. Rachel and R. Wiesendanger, Majorana quasiparticles in atomic spin chains on superconductors, *Physics Reports* **1099**, 1 (2025).
- [45] A. Y. Kitaev, Unpaired Majorana fermions in quantum wires, *Physics-Uspekhi* **44**, 131 (2001).
- [46] G. Jackeli and G. Khaliullin, Mott insulators in the strong spin-orbit coupling limit: From Heisenberg to a quantum compass and Kitaev models, *Phys. Rev. Lett.* **102**, 017205 (2009).
- [47] K. Yang, S. C. Morampudi, and E. J. Bergholtz, Exceptional spin liquids from couplings to the environment,

- Phys. Rev. Lett. **126**, 077201 (2021).
- [48] M. Kanega, T. N. Ikeda, and M. Sato, Linear and nonlinear optical responses in Kitaev spin liquids, Phys. Rev. Res. **3**, L032024 (2021).
- [49] W. Roberts, M. Vogl, and G. A. Fiete, Fidelity of the Kitaev honeycomb model under a quench, Phys. Rev. B **109**, L220406 (2024).
- [50] P. Molignini, A. G. Celades, R. Chitra, and W. Chen, Crossdimensional universality classes in static and periodically driven Kitaev models, Phys. Rev. B **103**, 184507 (2021).
- [51] G. Lindblad, On the generators of quantum dynamical semigroups, Commun.Math.Phys **48**, 119 (1976).
- [52] V. Gorini, A. Kossakowski, and E. C. G. Sudarshan, Completely positive dynamical semigroups of N-level systems, Journal of Mathematical Physics **17**, 821 (1976).
- [53] T.-S. Deng and L. Pan, Fate of symmetry protected coherence in open quantum system, Phys. Rev. B **104**, 094306 (2021).
- [54] C. A. Brasil, F. F. Fanchini, and R. d. J. Napolitano, A simple derivation of the Lindblad equation, Revista Brasileira de Ensino de Fisica **35** (2013).
- [55] D. A. Lidar, Lecture notes on the theory of open quantum systems (2020), arXiv:1902.00967 [quant-ph].
- [56] D. Manzano, A short introduction to the Lindblad master equation, AIP Advances **10**, 025106 (2020).
- [57] M. Žnidarič, Relaxation times of dissipative many-body quantum systems, Phys. Rev. E **92**, 042143 (2015).
- [58] Z. Cai and T. Barthel, Algebraic versus exponential decoherence in dissipative many-particle systems, Phys. Rev. Lett. **111**, 150403 (2013).
- [59] M. van Caspel and V. Gritsev, Symmetry-protected coherent relaxation of open quantum systems, Phys. Rev. A **97**, 052106 (2018).
- [60] N. Shibata and H. Katsura, Dissipative spin chain as a non-Hermitian Kitaev ladder, Phys. Rev. B **99**, 174303 (2019).
- [61] M. Žnidarič, Solvable quantum nonequilibrium model exhibiting a phase transition and a matrix product representation, Phys. Rev. E **83**, 011108 (2011).
- [62] J. Li, M. A. Sillanpää, G. S. Paraoanu, and P. J. Hakonen, Pure dephasing in a superconducting three-level system, Journal of Physics: Conference Series **400**, 042039 (2012).
- [63] M. V. Medvedyeva, F. H. L. Essler, and T. Prosen, Exact Bethe ansatz spectrum of a tight-binding chain with dephasing noise, Phys. Rev. Lett. **117**, 137202 (2016).
- [64] F. Tonielli, R. Fazio, S. Diehl, and J. Marino, Orthogonality catastrophe in dissipative quantum many-body systems, Phys. Rev. Lett. **122**, 040604 (2019).
- [65] P. E. Dolgirev, J. Marino, D. Sels, and E. Demler, Non-gaussian correlations imprinted by local dephasing in fermionic wires, Phys. Rev. B **102**, 100301 (2020).
- [66] O. Shtanko, A. Deshpande, P. S. Julienne, and A. V. Gorshkov, Complexity of fermionic dissipative interactions and applications to quantum computing, PRX Quantum **2**, 030350 (2021).
- [67] B. Misra and E. C. G. Sudarshan, The Zeno's paradox in quantum theory, Journal of Mathematical Physics **18**, 756 (1977).
- [68] V. V. Albert and L. Jiang, Symmetries and conserved quantities in Lindblad master equations, Phys. Rev. A **89**, 022118 (2014).
- [69] K. Kawabata, R. Sohal, and S. Ryu, Lieb-Schultz-Mattis theorem in open quantum systems, Phys. Rev. Lett. **132**, 070402 (2024).
- [70] M.-D. Choi, Completely positive linear maps on complex matrices, Linear Algebra and its Applications **10**, 285 (1975).
- [71] A. Jamiolkowski, Linear transformations which preserve trace and positive semidefiniteness of operators, Reports on Mathematical Physics **3**, 275 (1972).
- [72] D. Jaschke and L. D. Carr, Open source matrix product states: Exact diagonalization and other entanglement-accurate methods revisited in quantum systems, Journal of Physics A Mathematical General **51**, 465302 (2018).
- [73] M. Am-Shallem, A. Levy, I. Schaefer, and R. Kosloff, Three approaches for representing Lindblad dynamics by a matrix-vector notation (2015), arXiv:1510.08634 [quant-ph].
- [74] A. Sattler and M. Daghofer, Robustness of topological edge states in alternating spin chains against environment (2025), arXiv:2505.22420 [cond-mat.str-el].

Appendix A: Numerics

One numerical approach to solve the LME, see Eq. (3), is to reformulate it as an eigenvalue problem by utilizing the Choi-Jamiolkowski isomorphism [70, 71]. This technique, also known as vectorization, involves reshaping the density matrix into a vector by stacking its columns. The vectorized form of the LME [60, 72, 73] is given by

$$\begin{aligned} \frac{d}{dt}|\rho\rangle\rangle &= \mathcal{L}|\rho\rangle\rangle = \left[-i(\mathbb{1} \otimes H - H^T \otimes \mathbb{1}) \right. \\ &\left. + \gamma \sum_i \left((L_i^\dagger)^T \otimes L_i - \frac{1}{2} \left(\mathbb{1} \otimes L_i^\dagger L_i + (L_i^\dagger L_i)^T \otimes \mathbb{1} \right) \right) \right] |\rho\rangle\rangle, \end{aligned} \quad (\text{A1})$$

where H is the $n \times n$ Hamiltonian of the system, $\mathbb{1}$ denotes $n \times n$ identity matrix, \mathcal{L} is the $n^2 \times n^2$ Lindblad matrix, and $|\rho\rangle\rangle$ represents the vectorized density matrix. The solution to this differential equation is given by

$$|\rho(t)\rangle\rangle = e^{\mathcal{L}t} |\rho(0)\rangle\rangle = S e^{\Lambda t} S^{-1} |\rho(0)\rangle\rangle \quad (\text{A2a})$$

$$= \left[\sum_{m=0}^{\infty} \frac{1}{m!} \mathcal{L}^m t^m \right] |\rho(0)\rangle\rangle, \quad (\text{A2b})$$

where the initial density matrix at $t = 0$ corresponds to an eigenstate of the KHM. For small systems, we can perform full diagonalization (FD) of \mathcal{L} using Eq. (A2a), where S is the matrix of eigenvectors and Λ is a diagonal matrix comprising the eigenvalues of \mathcal{L} .

However, FD is computationally demanding. As an alternative, Eq. (A2b) can be employed to obtain solutions for larger systems [74]. This approach involves choosing a time step Δt and evaluating the power series expansion at $t = 0$ to compute $|\rho(\Delta t)\rangle\rangle$. The procedure is then iterated to successively determine $|\rho(2\Delta t)\rangle\rangle$, $|\rho(3\Delta t)\rangle\rangle$, and so forth. A suitable choice of parameters is a series expansion truncated at order $m_{\max} = 10$ with a time step $\Delta t = 0.1$. While in some cases lower orders (e.g., $m_{\max} = 5$) and larger time steps (e.g., $\Delta t = 0.5$) may suffice, these parameters are not generally reliable.

Since the dimension of the matrix \mathcal{L} scales as the square of the Hamiltonian's dimension (see Eq. (A2)), diagonalizing the Hamiltonian is significantly less computationally demanding than computing $|\rho(t)\rangle\rangle$. Consequently, utilizing FD for the Hamiltonian is sufficient.

Appendix B: Jump operators

Table I contains the definitions of the jump operators examined and indicates whether these operators lead to decoherence and whether they break or preserve the PHS of the BdG formalism. Table II lists the steady states and their degeneracies.

TABLE I. Definitions of the jump operator sets used in the LME are summarized. The leftmost column lists the labels for each set, while the adjacent column specifies the corresponding jump operators. Each set is constructed as a sum over the site index l , with uniform dissipation strength γ applied throughout. The third column indicates whether the jump operators induce decoherence, when this depends on Hamiltonian parameters, the specific conditions are provided. Here, $n \in \mathbb{Z}$. The rightmost column identifies whether the set breaks the BdG-type PHS. The notation used includes "pc" and "pa" for pair creation and pair annihilation operators, respectively, and "R" and "L" to denote hopping to the right (from the site $l+1$ to l) and to the left (from the site l to $l+1$), respectively.

label	jump operator	decoherence	BdG-type PHS
L_{n+k}	$L_l = \alpha_{(l,k)}^\dagger \alpha_{(l,k)}$	yes	broken if: $L \geq 2$ preserved if: $L = 1$
L_{n-k}	$L_l = \alpha_{(l,-k)} \alpha_{(l,-k)}^\dagger$	yes	broken if: $L \geq 2$: preserved if: $L = 1$
L_n	$L_l = \alpha_{(l,k)}^\dagger \alpha_{(l,k)} - \alpha_{(l,-k)} \alpha_{(l,-k)}^\dagger$	yes	preserved
L_{n+k}^+	$L_l^+ = \alpha_{(l,k)}^\dagger \alpha_{(l,k)}$	yes	preserved
L_{n-k}^-	$L_l^- = \alpha_{(l,-k)} \alpha_{(l,-k)}^\dagger$		
L_{pc}	$L_l = \alpha_{(l,k)}^\dagger \alpha_{(l,-k)}^\dagger$	$L = 1, J_z = 0$: yes $L = 1, J_z \neq 0, k = n\pi$: yes else: no	broken
L_{pa}	$L_l = \alpha_{(l,-k)} \alpha_{(l,k)}$	$L = 1, J_z = 0$: yes $L = 1, J_z \neq 0, k = n\pi$: yes else: no	broken
L_{p}	$L_l = \alpha_{(l,k)}^\dagger \alpha_{(l,-k)}^\dagger + \alpha_{(l,-k)} \alpha_{(l,k)}$	$J_x = J_z, k = 2\pi n$: no else: yes	preserved
$L_{\text{pc}}^{\text{pa}}$	$L_l^c = \alpha_{(l,k)}^\dagger \alpha_{(l,-k)}^\dagger$ $L_l^a = \alpha_{(l,-k)} \alpha_{(l,k)}$	yes	preserved
$L_{\text{J,R}}^{+k}$	$L_l = \alpha_{(l,k)}^\dagger \alpha_{(l+1,k)}$	no	broken
$L_{\text{J,L}}^{+k}$	$L_l = \alpha_{(l+1,k)}^\dagger \alpha_{(l,k)}$	no	broken
$L_{\text{J,L}}^{-k}$	$L_l = \alpha_{(l,-k)} \alpha_{(l+1,-k)}^\dagger$	no	broken
$L_{\text{J,R}}^{-k}$	$L_l = \alpha_{(l+1,-k)} \alpha_{(l,-k)}^\dagger$	no	broken
L_{J}	$L_l^{(1)} = \alpha_{(l,k)}^\dagger \alpha_{(l+1,k)}$ $L_l^{(2)} = \alpha_{(l+1,k)}^\dagger \alpha_{(l,k)}$ $L_l^{(3)} = \alpha_{(l,-k)} \alpha_{(l+1,-k)}^\dagger$ $L_l^{(4)} = \alpha_{(l+1,-k)} \alpha_{(l,-k)}^\dagger$	yes	preserved
L_{J}^{+k}	$L_l^{(1)} = \alpha_{(l,k)}^\dagger \alpha_{(l+1,k)}$ $L_l^{(2)} = \alpha_{(l+1,k)}^\dagger \alpha_{(l,k)}$	yes	preserved
L_{J}^{-k}	$L_l^{(1)} = \alpha_{(l,-k)} \alpha_{(l+1,-k)}^\dagger$ $L_l^{(2)} = \alpha_{(l+1,-k)} \alpha_{(l,-k)}^\dagger$	yes	preserved
$L_{\text{J,R}}$	$L_l^{(1)} = \alpha_{(l,k)}^\dagger \alpha_{(l+1,k)}$ $L_l^{(2)} = \alpha_{(l+1,-k)} \alpha_{(l,-k)}^\dagger$	no	preserved
$L_{\text{J,L}}$	$L_l^{(1)} = \alpha_{(l+1,k)}^\dagger \alpha_{(l,k)}$ $L_l^{(2)} = \alpha_{(l,-k)} \alpha_{(l+1,-k)}^\dagger$	no	preserved

TABLE II. Steady-state density matrices corresponding to the sets of jump operators defined in Tab. I are summarized. The steady state is the right eigenvector of \mathcal{L} (see Eq. (A1)) associated with the eigenvalue $\lambda_0 = 0$. When the steady state depends on Hamiltonian parameters, these conditions are specified in the "conditions" column. The variable $n \in \mathbb{Z}$. Here, $\text{diag}(\dots)$ indicates a diagonal matrix, and $\text{deg}(\lambda_0)$ denotes the degeneracy of the eigenvalue λ_0 . The maximally mixed state, as defined in Eq. (4), is represented by ρ_{mm} .

jump operators	conditions	$\text{deg}(\lambda_0)$	steady state
$L_{n+k}, L_{n-k}, L_n, L_{n-k}^{n+k}$	$L \geq 2, J_y \neq 0$	1	ρ_{mm}
	$L \geq 2, J_y = 0$	$\neq 1$	diagonal
	$L = 1, J_z \neq 0, k \neq n\pi$	1	ρ_{mm}
	$L = 1, J_z \neq 0, k = n\pi$	2	$\text{diag}(1, 0), \text{diag}(0, 1)$
	$L = 1, J_z = 0$	2	$\text{diag}(1, 0), \text{diag}(0, 1)$
L_{pc}	$L = 1, J_z = 0$	1	$\text{diag}(1, 0)$
	$L = 1, J_z \neq 0, k = n\pi$	1	$\text{diag}(1, 0)$
	$L \geq 2, J_y = 0$	$\neq 1$	non-diagonal
	else	1	non-diagonal
L_{pa}	$L = 1, J_z = 0$	1	$\text{diag}(0, 1)$
	$L = 1, J_z \neq 0, k = n\pi$	1	$\text{diag}(0, 1)$
	$L \geq 2, J_y = 0$	$\neq 1$	non-diagonal
	else	1	non-diagonal
L_{p}	$J_y \neq 0, J_x = J_z, k = 2\pi n$	$\neq 1$	non-diagonal
	$L \geq 2, J_y = 0$	$\neq 1$	non-diagonal
	else	1	ρ_{mm}
$L_{\text{pc}}^{\text{pa}}$	$L \geq 2, J_y = 0$	$\neq 1$	non-diagonal
	$L \geq 2, J_y \neq 0$	1	ρ_{mm}
	$L = 1$	1	ρ_{mm}
$L_{\text{J,R}}^{+k}, L_{\text{J,L}}^{+k}, L_{\text{J,L}}^{-k}, L_{\text{J,R}}^{-k}$	$J_y \neq 0$	1	non-diagonal
	$J_y = 0$	$\neq 1$	non-diagonal
$L_{\text{J,R}}, L_{\text{J,L}}$	$J_y \neq 0$	1	non-diagonal
	$J_y = 0$	$\neq 1$	non-diagonal
$L_{\text{J}}, L_{\text{J}}^{+k}, L_{\text{J}}^{-k}$	$J_y \neq 0$	1	ρ_{mm}
	$J_y = 0$	$\neq 1$	non-diagonal